

Trapping of Single Atoms in Metasurface Optical Tweezer Arrays

Aaron Holman¹, * Yuan Xu², * Ximo Sun¹, Jiahao Wu², Mingxuan Wang¹, Bojeong Seo¹, Nanfang Yu², † and Sebastian Will¹‡

¹*Department of Physics, Columbia University, New York, New York 10027, USA and*

²*Department of Applied Physics and Applied Mathematics,
Columbia University, New York, New York 10027, USA*

(Dated: November 11, 2024)

Optical tweezer arrays have emerged as a key experimental platform for quantum computation, quantum simulation, and quantum metrology, enabling unprecedented levels of control over single atoms and molecules. Existing methods to generate tweezer arrays mostly rely on active beam-shaping devices, such as acousto-optic deflectors or liquid-crystal spatial light modulators. However, these approaches have fundamental limitations in array geometry, size, and scalability. Here we demonstrate the trapping of single atoms in optical tweezer arrays generated via holographic metasurfaces. We realize two-dimensional arrays with more than 250 tweezer traps, arranged in arbitrary geometries with trap spacings as small as 1.5 μm . The arrays have a high uniformity in terms of trap depth, trap frequency, and positional accuracy, rivaling or exceeding existing approaches. Owing to sub-micrometer pixel sizes and high pixel densities, holographic metasurfaces open a path towards optical tweezer arrays with $> 100,000$ traps.

Optical tweezer arrays have led to a revolution in the control of ultracold atoms and molecules for quantum applications [1]. They have broken new ground for quantum simulation [2] and quantum computation [3, 4], including the realization of quantum spin systems [5, 6], high-fidelity Rydberg quantum gates [7–9], and first steps towards error-corrected quantum computation [10]. Recently, dual species atomic arrays [11, 12] and arrays of dipolar molecules have also been reported [13, 14]. Optical tweezer arrays enable new approaches for quantum metrology, such as optical tweezer clocks [15, 16], and hold great promise for novel experiments in quantum optics, including explorations in cavity quantum electrodynamics [17] and correlated atom-photon interactions [18–20].

The ability to generate high-quality optical tweezer arrays is a central requirement for many experiments. A tweezer array consists of numerous tightly focused laser beams, each constituting a trap for a single particle. Key criteria include high flexibility in array geometry, trap uniformity, and scalability. In addition, compactness, robustness, and high optical efficiency are desirable, especially with the prospect of deploying tweezer-based quantum devices outside of controlled laboratory environments [21–23]. Currently, optical tweezer arrays are mostly generated via active beam-shaping devices, such as acousto-optical deflectors (AODs) [24, 25], liquid crystal spatial light modulators (SLMs) [26, 27], or digital micromirror devices (DMDs) [28]. These devices require complex control electronics and projection optics with high numerical aperture (NA) to relay the tweezer arrays onto ultracold atoms and molecules. Technical complexity and fundamental limitations constrain array sizes to $< 10,000$ traps, which has started to impose a limit on the quantum applications that can be pursued. Alternative techniques, such as amplitude masks [29] and microlens arrays [30], have been explored, but limited beam-shaping capabilities make it chal-

lenging to achieve highly uniform arrays.

In recent work [31], we proposed holographic metasurfaces as a new approach to generate versatile and scalable tweezer arrays. Metasurfaces are flat optical devices comprised of sub-micrometer pixels that can imprint an arbitrary phase mask onto an incident laser beam [32–34], both generating and focusing an optical tweezer array. Metasurfaces feature high power handling capabilities [35], diffraction-limited focusing [36], and comprehensive polarization control [37, 38]. A recent experiment demonstrated single atom trapping in a 3×3 tweezer array that was generated with an AOD and focused down by a metasurface lens [39]; however, a demonstration of atomic tweezer arrays that utilize the full beam-shaping capabilities of metasurfaces – array generation and focusing – has so far been elusive.

In this work, we demonstrate the trapping of single strontium (Sr) atoms in metasurface optical tweezer arrays. Using laser light at a wavelength of 520 nm, we realize two-dimensional arrays with arbitrary geometries, both periodic and non-periodic, with more than 250 traps and trap spacings as small as 1.5 μm . We find the trap uniformity to be comparable to state-of-the-art techniques and demonstrate single-atom preparation and detection with high fidelity. The holographic metasurfaces in this work have sub-micrometer and subwavelength pixel sizes, offering a realistic path towards array sizes beyond 100,000 traps, and thus overcoming fundamental limitations of existing beam-shaping approaches.

METASURFACES FOR OPTICAL TWEEZERS

Metasurfaces have emerged as a powerful platform for the manipulation of optical waves [40, 41]. They enable holographic control of incident light fields by manipulating the amplitude and phase of an optical wavefront in the device plane. Metasurfaces are comprised of a matrix of nano-etched meta-atoms that serve as control pixels; the meta-atoms are selected from a library – a collection of scatterers with different shapes and sizes – and carefully positioned to engineer the optical wavefront that leads to the desired pattern in the imaging

* These authors contributed equally.

† ny2214@columbia.edu

‡ sebastian.will@columbia.edu

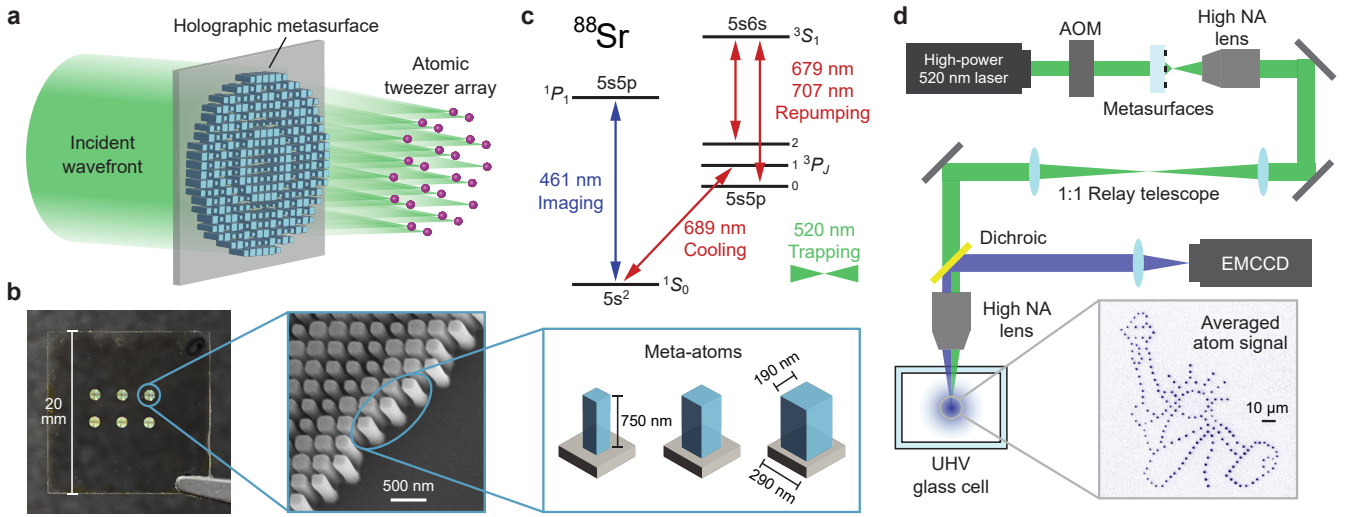


Fig. 1. Metasurface optical tweezer arrays and integration with ultracold strontium atoms. **a**, Illustration of the working principle of a holographic metasurface. The metasurface imprints a phase pattern on an incident collimated Gaussian laser beam and produces a two-dimensional array of tight tweezer traps at the focal plane. In this work, the focal length of the metasurfaces is 0.7 mm and the effective NA is > 0.6 . **b**, (left) Photograph of a substrate holding 6 metasurfaces, each with a distinct tweezer array pattern. The substrate has a size of 20 mm \times 20 mm. The metasurfaces have a diameter of 1.16 mm. (middle) Scanning electron microscope image of a portion of a metasurface. (right) The meta-atoms have a unit cell size of 290 nm, are 100–190 nm wide, and 750 nm tall. They are chosen from a predetermined library to introduce a wide range of phase delays to the incoming beam without modifying its amplitude. **c**, Level diagram of ^{88}Sr showing the optical transitions relevant to this work. Atoms are cooled and imaged on the broad transition at 461 nm in conjunction with the repumpers at 679 nm and 707 nm. Narrow-line cooling on the intercombination line at 689 nm (linewidth 7.5 kHz) creates Sr samples at microkelvin temperatures. **d**, Schematic of the setup to trap and image atoms. The tweezer laser operates at 520 nm. Its intensity is controlled with an acousto-optic modulator (AOM) before illuminating the metasurface. The metasurface generates and focuses the tweezer array, which is collimated by a high-NA microscope objective, relayed via a 1:1 telescope, and focused down with a high-NA objective into the ultra-high vacuum glass cell to trap atoms. During imaging, fluorescence photons of the atoms are detected with a single-photon sensitive camera.

plane. Each meta-atom is a few hundred nanometers wide and tall, smaller than the wavelength of the light they manipulate. Metasurfaces can be fabricated on the millimeter to centimeter scale [42, 43] with well over 10^6 pixels. Because of the sub-wavelength size of the meta-atoms, metasurfaces can achieve high spatial resolution and forward-scattering efficiency.

We use transmitting metasurfaces for visible light at 520 nm (Fig. 1a). These metasurfaces are phase-only modulating masks designed using a Gerchberg-Saxton algorithm-based optimization approach (see Methods for details). The optimized metasurface encodes a phase pattern that simultaneously generates and focuses a tweezer array. Multiple metasurfaces are placed on a single substrate (Fig. 1b), allowing for easy switching between distinct designs and their associated tweezer arrays by translation of the substrate. The metasurfaces are fabricated using standard cleanroom protocols from thin films of silicon-rich silicon nitride (SRN). This material is chosen for its high optical refractive index and ease of manufacturing (see Methods for additional considerations). To minimize alignment sensitivity and mitigate diffraction effects of the Gaussian input beam at the metasurface boundaries, the metasurface is manufactured with a circular footprint and assumes the incidence of a plane wave onto the device. The metasurfaces have a diameter of 1.16 mm and 2.32 mm. They can handle optical intensities up to 25 W/mm^2 without active cooling, have a diffraction efficiency of $\sim 60\%$, and an

effective NA of > 0.6 . Additional details on the design and optimization of the metasurface hologram, meta-atom library, cleanroom fabrication procedure, and optical properties are provided in the Methods.

The optical tweezer arrays are projected into the glass cell of an ultrahigh-vacuum chamber (see Methods for details). A schematic of the projection system is shown in Fig. 1d. Before illuminating the metasurface, a laser at 520 nm passes through an acousto-optic modulator (AOM) for fast switching and trap depth control. The substrate with the metasurfaces is mounted on a two-axis translation stage, allowing for rapid switching between different array geometries with minimal realignment. The tweezer array, generated by the metasurface at the focal plane, is converted into the optical momentum space by a microscope lens (NA = 0.6), relayed through a 1:1 telescope, and converted back into the tweezer array in the glass cell by an objective lens (NA = 0.5). Tweezer generation with an AOD, liquid crystal SLM, or DMD typically requires demagnification optics with large-diameter lenses that are prone to aberrations. Due to the high NA of the metasurface, demagnification is not necessary. In principle, metasurfaces can directly trap atoms at their focal plane (e.g., by placing them inside or near the vacuum chamber) without the need for additional relay optics.

We load atoms into the metasurface optical tweezer array from an ultracold cloud of ^{88}Sr . The strontium atoms are

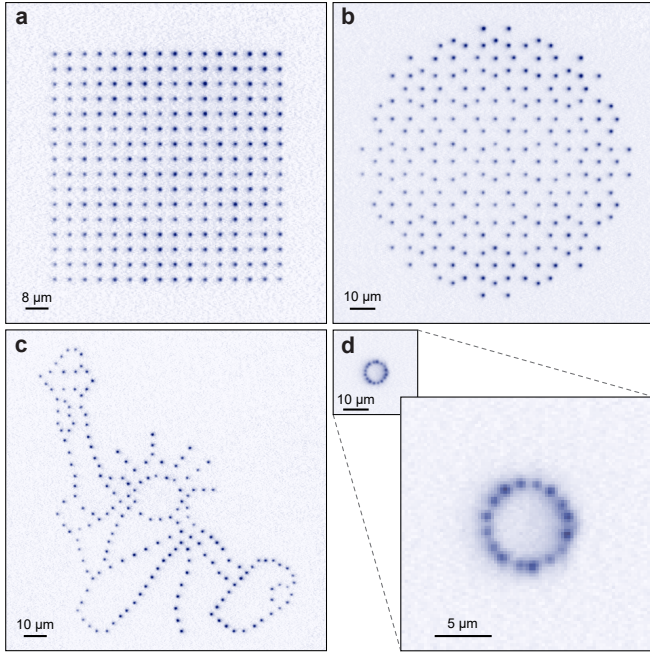


Fig. 2. Fluorescence images of strontium atoms trapped in metasurface-generated optical tweezer arrays. Each image is an average of 100 individual images without parity projection. **a**, Square lattice with 256 traps, average spacing of 4 μm . **b**, Quasicrystal (Penrose tiling) with 225 traps, average spacing of 4 μm . **c**, Statue of Liberty pattern with 183 traps, average spacing of 3 μm . **d**, Necklace pattern with 16 traps, average spacing of 1.45 μm .

cooled to microkelvin temperatures using standard techniques that leverage strontium's unique level structure (Fig. 1c). Subsequently, the trapped atoms are detected via fluorescence imaging (see Methods). Figure 2 shows fluorescence images of atoms in different metasurface-generated tweezer arrays, including a periodic 16×16 pattern, a quasicrystal pattern (Penrose tiling), a fully arbitrary pattern, and a necklace pattern with close tweezer spacing on the micrometer-scale.

SINGLE ATOM TRAPPING AND IMAGING

We demonstrate single-atom trapping and detection in a 4×4 metasurface array (see Fig. 3). The steps to achieve this are highly sensitive to the quality and uniformity of the optical tweezer potential. The initial loading of the array is statistical; each trap is occupied by at least one atom, but the precise number of atoms is random. In the next step, we perform parity projection: traps that initially have an odd (even) number of atoms are turned into sites with one (no) atom. This is achieved via photoassociation into an electronically excited Sr_2 molecular state, close to the 689 nm atomic resonance, which induces pairwise atom loss [44]. After parity projection, 49(3)% of the traps contain an atom, as shown in Fig. 3b.

To determine the occupation in the array, we perform fluorescence imaging on the 461 nm transition, while keeping the atoms trapped. Fluorescence photons are collected with

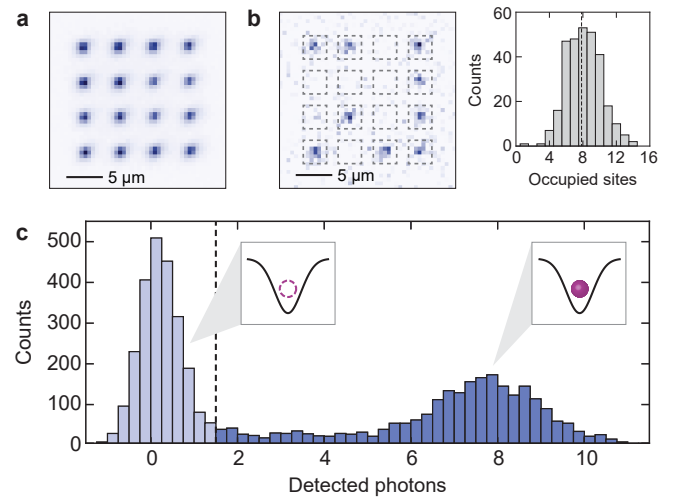


Fig. 3. Single atom preparation and detection in a 4×4 metasurface array. **a**, Average of 100 fluorescence images after parity projection. The uniformity indicates that all traps have an approximately equal chance of being filled with an atom. **b**, (left) Individual fluorescence image. Trap locations are indicated by dashed boxes. (right) Histogram of the number of occupied sites after parity projection; the mean occupancy of a trap, marked by the dashed line, is 49(3)%. **c**, Histogram of photon counts in the trap locations of the 4×4 array, as marked in **b**. 500 repetitions of the experiment are averaged. The data allows for the distinction between sites with one and zero atoms with high fidelity. The dashed line marks the threshold value, determined as discussed in Methods.

a low-noise camera and the photon number in the trap locations (marked in Fig. 3b, left panel) is evaluated. To maximize the number of photons scattered per atom, we simultaneously cool via repulsive Sisyphus cooling [45] on the 689 nm, $m_J = \pm 1$ transition, counteracting the recoil heating from repeated photon scattering on the 461 nm transition. Figure 3c shows a histogram of the detected photon numbers in the trap locations. The histogram shows two peaks: one peak centered on zero photons, corresponding to zero atoms, and a second peak centered on ~ 8 photons, corresponding to the presence of a single atom. The absence of photon counts above the single-atom peak indicates the high efficiency of parity projection. The presence of photon counts between the zero- and single-atom peaks results from loss of Sr atoms during imaging in 520 nm traps. Similar observations were reported in Ref. [46]. We attribute this loss to an ionization process out of the ${}^3\text{P}_1$ state, which is populated during Sisyphus cooling. This will be analyzed in further detail in future work. For alternative trapping wavelengths, for example 813 nm [47], such losses are known to be absent. Using a model-free approach that involves the recording of two fluorescence images in short sequence [48], we determine the imaging fidelity to be $> 99.8(5)\%$ (see Methods).

CHARACTERIZATION OF ARRAY QUALITY

Next, we characterize the uniformity of a 16×16 array. We use the trapped atoms as highly sensitive probes to measure the depth, frequency, and position of each trap. A high uniformity in trap depth and frequency ensures that the light shift and on-site vibrational modes are constant across the array. These characteristics are important for sideband cooling, atomic state preparation, and spectrally sensitive operations, such as atomic quantum gates and interrogation of clock states. A high accuracy of trap positions is desirable for the precise control of atom-atom interactions, for example, in Rydberg arrays and correlated atom-photon interactions.

We characterize the uniformity of trap depth by measuring the resonance frequency of the narrow Sr intercombination transition at 689 nm in each tweezer. The resonance is shifted away from the free-space resonance due to a differential light shift between the 1S_0 and the 3P_1 states in the 520 nm trapping field. While keeping the overall laser intensity fixed, the 689 nm resonance is measured in each trap via loss spectroscopy. From this, we determine the local light shift, which, with the knowledge of the polarizability of 1S_0 and 3P_1 , is converted into a trap depth. As shown in Fig. 4a, we find a mean trap depth of 0.52 mK with a standard deviation of 7.5% across the array.

The trap frequencies of individual tweezers are measured via parametric driving, both in the radial and axial directions. The intensity of the tweezer light is modulated sinusoidally with an amplitude of 5% for 30 ms while the frequency of the modulation is varied. A parametric resonance is observed via atom loss at twice the trap frequency. Averaged over the array, we measure a mean radial (axial) trap frequency of 105 kHz (14 kHz) with a standard deviation of 5% (8%). Figure 4b shows the data for the radial trap frequency. The data for the axial trap frequency is shown in Extended Data Fig. 7.

To characterize the spatial accuracy, we compare the measured trap locations with the target trap positions that were used for the design of the metasurface. Fitting each atom's fluorescence signal to a 2D Gaussian, we extract the tweezer locations. The positional inaccuracy between intended and measured locations is defined as $\Delta r = \sqrt{\Delta x^2 + \Delta y^2}$, where Δx (Δy) is the deviation in the x (y) direction. We find a mean deviation of 60 nm, as shown in Fig. 4c. Compared with the trap spacing of 4 μm , this corresponds to a positional inaccuracy on the 1.5% level. The deviation is comparable to the extent of the ground-state vibrational wavefunctions of Sr of about 30 nm and 90 nm in the radial and axial direction, respectively.

The uniformity of trap depth, frequency, and position of the metasurface approach rivals or exceeds the performance of existing techniques. For example, arrays generated with liquid crystal SLMs often have trap depth fluctuations of 10% to 20% [27, 49, 50], while methods to further reduce such fluctuations via feedback are under active research [51, 52]. For the metasurface arrays, we attribute the remaining non-uniformity to imperfections in the optical relay optics and to fabrication errors of meta-atoms, both of which have considerable room for improvement. Prior to transmission through the relay optics, we measure an intensity non-uniformity at the focal plane

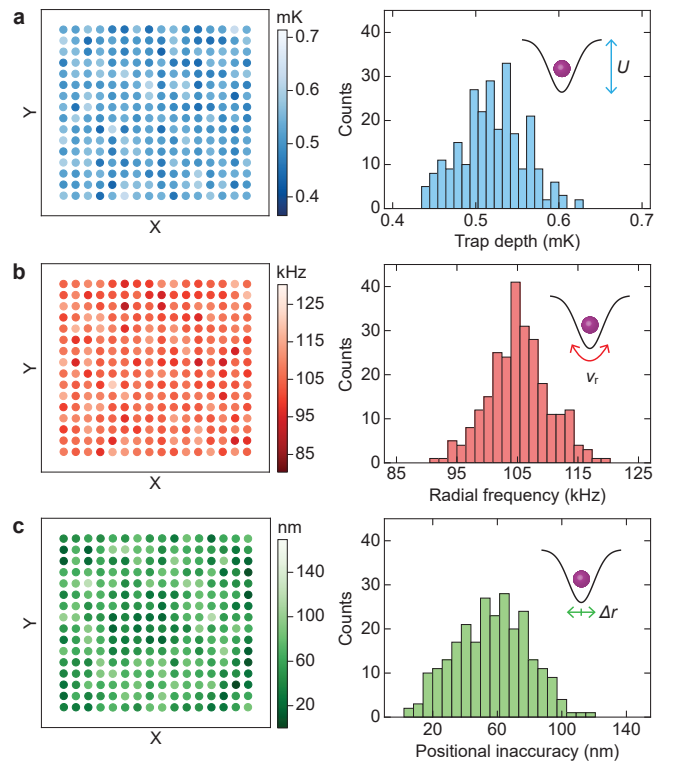


Fig. 4. Characterizing the uniformity of metasurface arrays via atomic response. A square array with 16×16 traps and a $4 \mu\text{m}$ trap spacing is used. The uniformity in terms of **a**, trap depth, U , **b**, radial trap frequency, v_r , and **c**, trap positions is characterized for each trap in the array (left column). Histograms of the respective quantities observed for each trap (right column).

of the metasurface as low as 4% (see Methods).

SCALABILITY OF METASURFACE OPTICAL TWEEZER ARRAYS

In this section, we discuss the scalability of metasurface optical tweezer arrays and show how their performance compares to other pixel-based beam shaping devices, such as DMDs and liquid crystal SLMs. We find that pixel size and number have a significant impact on the ability to create large and uniform tweezer arrays.

To illustrate this point, we first consider reproducing a simple lens with a pixel-based device, as shown in Fig. 5a. The pixel size is denoted by d , the pixel density is $1/d$, and the wavelength of the incident laser beam is denoted by λ . We first convert a spherical lens to a Fresnel lens by taking the phase profile $\phi(x)$ of the former, modulo 2π . When the phase profile of the Fresnel lens is approximated with a pixel-based device, the finite sampling constrains the steepness of phase gradients that can be reproduced, $\partial\phi/\partial x \lesssim \pi/2d$. This limits the ability to reproduce steep phase gradients at the edge of the lens. A larger pixel size will reduce the attainable phase gradient, reducing the usable diameter of the device, and effectively reducing the NA that can be achieved. Based on this

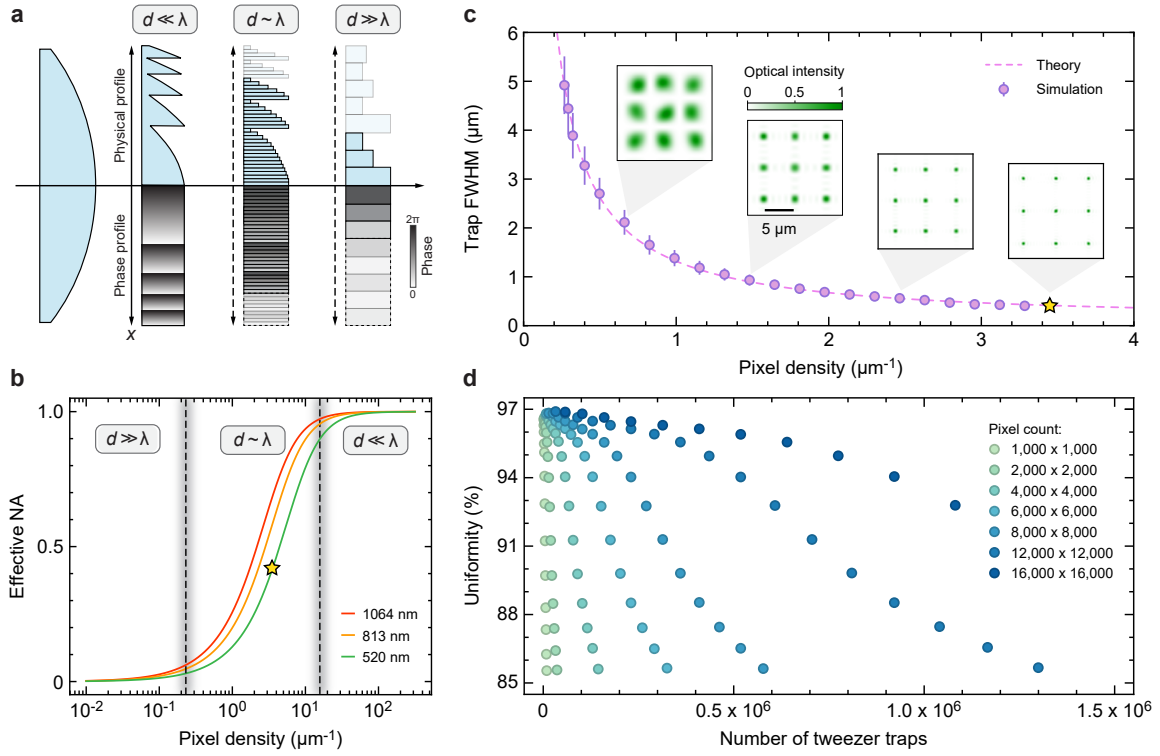


Fig. 5. Performance of pixel-based beam shaping devices. **a**, Approximation of the phase profile of a spherical lens with infinitely small pixel size ($d \ll \lambda$), intermediate pixel size ($d \sim \lambda$), and large pixel size ($d \gg \lambda$). For larger pixel sizes, the reproduction of steeper phase gradients $\partial\phi/\partial x$ is limited. This limits the usable diameter of the device and reduces the effective NA. **b**, Effective NA of a lens generated with a pixel-based device as a function of pixel density $1/d$ for common trapping wavelengths λ . The dashed vertical lines indicate the approximate separation between the regimes $d \ll \lambda$, $d \sim \lambda$, and $d \gg \lambda$. The yellow star indicates the pixel density for the metasurfaces used in this work. **c**, Focusing capabilities of pixel-based beam shaping devices. For a laser wavelength of 520 nm, a fixed device resolution of 300×300 pixels, and varying pixel density $1/d$, an optimized 3×3 square array with 5 μm spacing is generated (insets) (further details in Methods). Data points show the tightness of the traps, measured as the FWHM. Error bars show the standard deviation across the array. The pixel densities range from state-of-the-art liquid crystal SLMs ($d = 4 \mu\text{m}$) to the holographic metasurface used in this work (yellow star, $d = 290 \text{ nm}$). The dashed line shows a fit of the effective NA model (further details in Methods). **d**, Simulation of the uniformity of trap intensity as a function of the number of tweezer traps for device resolutions ranging from $1,000 \times 1,000$ (light green) to $16,000 \times 16,000$ (dark blue) pixels (square-shaped device). Uniformity is defined as 100% minus the standard deviation of the trap intensity across the array (in %). The simulation assumes a pixel size of $d = 290 \text{ nm}$ (further details in Methods).

argument, we derive an approximate analytical expression for the effective numerical aperture attainable for a given pixel size, $\text{NA} = 1/\sqrt{1 + (4d/\lambda)^2}$ (see Methods for details). In Fig. 5b, we plot the effective NA for a broad range of pixel densities and several common tweezer wavelengths in the visible and near-infrared, illustrating that a smaller pixel size relative to the laser wavelength can lead to a dramatically increased effective NA. For a pixel size of several μm (typical for DMDs and liquid crystal SLMs), in the regime $d \gg \lambda$, the NA is limited to below 0.05. For subwavelength pixels, in the regime $d \lesssim \lambda$, NAs of 0.5 and higher can be reached.

Going beyond the example of a lens, we simulate optical tweezer arrays that can be generated with a pixel-based device (see Fig. 5c). For a smaller pixel size d , the effective NA attainable is higher, and thus the individual tweezers can be focused more tightly. This enhances the quality of the individual tweezers and allows the metasurfaces to accommodate more tweezer traps in the same area. In a series of simula-

tions, we vary the pixel size d , but keep the device pixel count at 300×300 , while optimizing the phase mask to generate a 3×3 square array of traps with 5 μm spacing in the focal plane (see Methods). As shown in Fig. 5c, the full-width-half-maximum (FWHM) of the traps steadily decreases as the pixel density $1/d$ increases. As a result, holographic metasurfaces with subwavelength pixels can generate optical tweezer arrays that are sufficiently tight at the focal plane for direct trapping of atoms, while devices with larger pixels require additional demagnification optics.

Because of the small pixel sizes of holographic metasurfaces, a large number of pixels can be accommodated in a relatively small device footprint. This is advantageous as the number of high-quality traps that can be generated is positively correlated with the number of available pixels. To quantify this relation, we consider devices with pixel counts ranging from $1,000 \times 1,000$ (10^6) to $16,000 \times 16,000$ (256×256) and investigate the uniformity of trap intensity across the array as a function of the number of tweezer traps (see Methods).

The results in Fig. 5d show that for a fixed pixel count, the uniformity drops monotonically when the required number of traps increases. The results also suggest a rule-of-thumb that ~ 300 pixels are needed to produce one high-quality tweezer trap in an array. For example, the number of highly uniform (uniformity $> 95\%$) tweezer traps that can be generated by a top-end SLM with 4000×4000 pixels will be fundamentally limited to $\sim 50,000$; the 2.32 mm metasurface in this work contains $\sim 8000 \times 8000$ pixels, allowing the creation of 200,000 highly uniform tweezer traps, provided that sufficient laser power is available.

CONCLUSIONS

In this work, we have demonstrated single-atom trapping in metasurface optical tweezer arrays. We show that the uniformity of the arrays is comparable to that realized using existing methods; further improvements are expected via optimized fabrication and system integration. Because of subwavelength pixel sizes, holographic metasurfaces can reach a high effective NA. This allows for the creation of tightly focused tweezer arrays at the metasurface's focal plane, enabling direct trapping of atoms without the need for demagnification or relay optics. Because of high pixel counts [43] and high power handling capabilities [35], metasurfaces offer a realistic path towards atomic tweezer arrays with $> 100,000$ sites, overcoming fundamental limitations of existing approaches. This addresses a critical need for future applications in quantum simulation, quantum computing, quantum sensing, and optical clocks based on atomic arrays.

We envision future extensions of the metasurface optical tweezer array platform. By combining the static arrays demonstrated here with a dynamic sorting beam, it will become possible to rearrange atoms and create unity filled arrays. In addition, metasurfaces can be functionalized in various ways: resonant metasurfaces [53] can be designed to only impart a phase pattern on light within a narrow spectral band. This will enable the creation of metasurface stacks, comprised of several metasurfaces for different spectral bands, through which atomic arrays can be generated, sorted, and imaged. Additionally, metasurfaces can be designed to produce the exact same array pattern at different wavelengths, which may prove useful for both single- and dual-species atomic tweezer systems [11, 12]. Furthermore, polarization sensitive metasurfaces offer an additional tuning knob [31]. Finally, the passive stability and compactness of metasurfaces offers a robust platform for field-deployable atomic tweezer quantum devices.

ACKNOWLEDGMENTS

We are grateful to Xiaoyan Huang and Weijun Yuan for contributions in the early development of this project and Stephanie C. Malek for help with the development of the SRN material platform. We thank Chun-Wei Liu and Siwei Zhang for experimental assistance, and Dmytro Filin and Marianna Safronova for providing data on the optical polarizabil-

ity of Sr atoms. We thank Ana Asenjo-Garcia, Stuart Masson, and Ricardo Gutierrez-Jauregui for fruitful discussions, and Tarik Yefsah for critical reading of the manuscript. This work was supported by the National Science Foundation (Award nos. 1936359, 2040702, and 2004685) and the Air Force Office of Scientific Research (Award nos. FA9550-16-1-0322 and FA9550-23-1-0404). Device fabrication was carried out at the Columbia Nano Initiative cleanroom, at the Advanced Science Research Center Nanofabrication Facility at the Graduate Center of the City University of New York, and at the Center for Functional Nanomaterials, Brookhaven National Laboratory, supported by the US Department of Energy, Office of Basic Energy Sciences (Contract no. DESC0012704). B.S. acknowledges support from the National Research Foundation of Korea (Award no. 2021M3H3A1036573). S.W. acknowledges support from the Alfred P. Sloan Foundation.

AUTHOR CONTRIBUTIONS

All authors contributed substantially to the work presented in this paper. A.H., X.S., M.W., and B.S. carried out the atomic experiments. Y.X. and J.W. designed and fabricated the metasurfaces. N.Y. and S.W. supervised the study. All authors contributed to the data analysis and writing of the paper.

METHODS

MATERIAL PLATFORM FOR VISIBLE-SPECTRUM METASURFACES

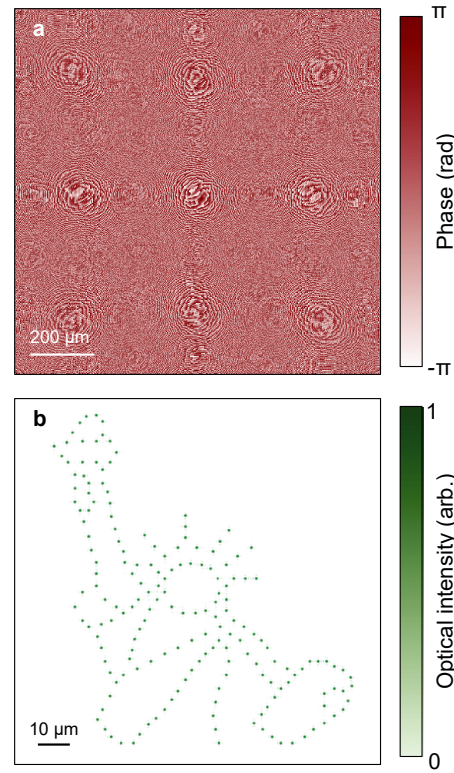
To fabricate holographic metasurfaces operating at a wavelength of $\lambda = 520$ nm, titanium dioxide (TiO_2) is frequently selected due to its high refractive index and minimal absorption [54, 55]. Various methods have been explored for creating TiO_2 -based metasurfaces, such as atomic layer deposition (ALD) on patterned electron-beam (e-beam) resist [54] or employing inductively coupled plasma (ICP) etching with a patterned chromium (Cr) mask [31]. However, these methodologies face significant scalability and integration challenges within complementary metal-oxide-semiconductor (CMOS) workflows due to the slow deposition rates of ALD or the ICP etching of TiO_2 and eventual removal of Cr masks.

Considering these challenges, we employ a novel material platform, silicon-rich silicon nitride (SRN), to fabricate our metasurfaces. SRN has been used to build nonlocal metasurfaces with great performance and excellent wavelength selectivity, enabled by photonic resonances in the visible spectrum [56]. We utilize plasma-enhanced chemical vapor deposition (PECVD) to deposit SRN films onto optically thick fused silica substrates. This enables precise control over the real part of the linear refractive index of SRN films, which can be adjusted from 1.92 to 3.1 by varying the ratios of the precursor gases (SiH_4 , N_2 and NH_3) used in the PECVD process [57]. Such tunability provides the flexibility required to accommodate a wide range of functionalities. For our specific application at $\lambda = 520$ nm, we deposit SRN films with a real part of the refractive index of 2.3 and an imaginary part maintained near zero. This greatly enhances the design possibilities for these metasurfaces while ensuring high transmission and high diffraction efficiency.

CALCULATION AND OPTIMIZATION OF PHASE-ONLY HOLOGRAMS

To compute the phase-only holograms used to create arbitrary trap arrays with a designated focal length and NA, we employ a Gerchberg-Saxton algorithm-based approach [58]. The original algorithm utilizes the Rayleigh-Sommerfeld diffraction integral to iterate between the diffractive optical elements (DOE) plane (in our case, the metasurface plane) and the focal plane by forward and backward light propagation. This iterative process ultimately determines the phase profile necessary to generate the desired pattern. In each iteration, the input amplitude at the metasurface plane is set to unity, enforcing a phase-only condition for the algorithm. An example of the resulting phase-only hologram and the corresponding simulated trap array pattern is shown in Extended Data Fig. 1.

However, the standard Gerchberg-Saxton algorithm is designed for general holography and inevitably introduces speckle and noise into the resulting patterns. Although this can be mitigated by using soft operations when updating the

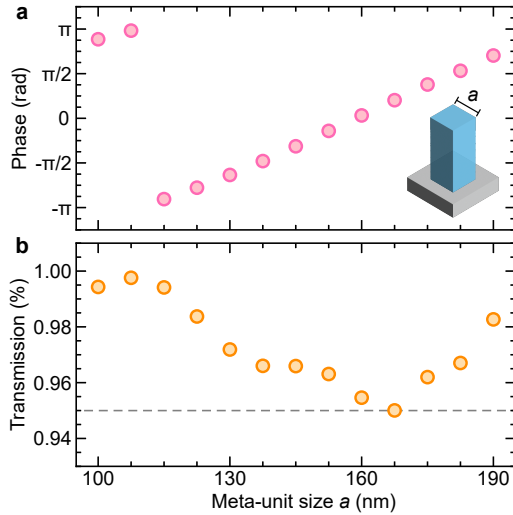


Extended Data Fig. 1. A calculated phase-only hologram and its corresponding focal plane trap pattern. **a**, A phase-only hologram generated by the modified Gerchberg-Saxton algorithm with $4,000 \times 4,000$ pixel resolution and a 290 nm pixel size. **b**, Simulated intensity distribution at the focal plane, which shows the Statue of Liberty made of 183 traps as designed.

hologram [59], achieving high-quality, point-like traps remains a significant challenge. To address this, we employ a weighted Gerchberg-Saxton (GSW) algorithm [60], modified to account for the subwavelength pixel size and the direct focusing capability of our meta-holograms. At the $(k+1)^{\text{th}}$ iteration, the target amplitude distribution is determined by the simulated focal plane amplitude and the target amplitude from the previous iteration via

$$A_{\text{target}}^{k+1}(x, y) = \frac{A_{\text{target}}^k(x, y)}{A_{\text{simulated}}^k(x, y)},$$

where $A_{\text{target}}^{k+1}(x, y)$ and $A_{\text{target}}^k(x, y)$ represent the target amplitude distributions at the $(k+1)^{\text{th}}$ and k^{th} iterations, respectively, and $A_{\text{simulated}}^k$ is the simulated focal plane amplitude. To prevent the target amplitude from producing extreme numerical values, numerical normalization and soft operations are performed in each update. Through this approach, we can generate high-quality phase-only holograms capable of producing near-uniform point trap arrays in arbitrary geometries, with a simulated standard deviation below 3% even for arrays consisting of hundreds of traps.



Extended Data Fig. 2. RCWA-simulated phase response and transmission of the selected meta-unit library. **a**, Phase response of the meta-unit library as a function of pillar width a . **b**, Transmission of the meta-unit library. All individual meta-units have a transmission over 95% (marked as the grey dashed line).

META-UNIT LIBRARY DESIGN

To construct the meta-unit library for our metasurfaces, we utilize rigorous coupled-wave analysis (RCWA) simulations to determine the phase and amplitude response of individual SRN nanopillars. By using non-birefringent meta-units and constraining the meta-units to square-shaped cross-sections, we maximize the metasurfaces' diffraction efficiency while minimizing fabrication defects.

The pitch between the nanopillars (pixel size) is set to 290 nm. The height of the nanopillars is set to 750 nm and their width ranges from 100 to 190 nm, which provides comprehensive phase coverage over the 2π range while maintaining near unity transmission. The subwavelength size enables an achievable numerical aperture (NA) of up to 0.9, allowing great flexibility in designing the phase hologram. Extended Data Fig. 2 shows the RCWA-simulated phase and amplitude response for the selected meta-unit library, which consists of 14 SRN nanopillars of varying square cross-sectional sizes, all with a uniform height of 750 nm. Due to the subwavelength pixel size, this small library is sufficient to achieve fine-grained phase control across a λ^2 area. To prevent defects caused by missing or collapsed pillars during fabrication, the smallest pillar is designed with a minimum edge width of 100 nm. The library achieves a high overall transmission that exceeds 95% across the entire set of meta-units, resulting in an experimental diffraction efficiency of over 60%.

FABRICATION OF SRN METASURFACES

The metasurfaces presented in this work are manufactured through a CMOS-compatible nanofabrication process, as il-

lustrated in Extended Data Fig. 3a. A 750 nm thick SRN layer, with a designed refractive index of 2.3, is deposited onto 500 μ m thick fused silica wafers, which are subsequently diced into square pieces with a diagonal length of 1 inch to fit standard optical mounts in the experimental setup. A two-layer resist (PMMA 495k A4 and 950k A2) is spun-coated onto the SRN layer, and electron beam lithography (EBL; Elionix ELS-G100) is performed with a dose of $770 \mu\text{C}/\text{cm}^2$ and a current of 2 nA. To prevent the electron charging effect caused by the non-conductive substrate during the EBL process, a 20-nm E-spacer is spun-coated onto the chip. After exposure, the resist is developed in a mixed solution of IPA:DI water = 3:1 for 2 minutes. The developed resist is then coated with a 25 nm thick Al_2O_3 layer using electron beam evaporation to serve as a hard mask for etching. The mask is subsequently lifted off in Remover PG overnight, leaving the patterned region on the SRN layer. This pattern is etched into the SRN film to form SRN nanopillars using an inductively coupled plasma (ICP) etching system (Oxford PlasmaPro 100 Cobra).

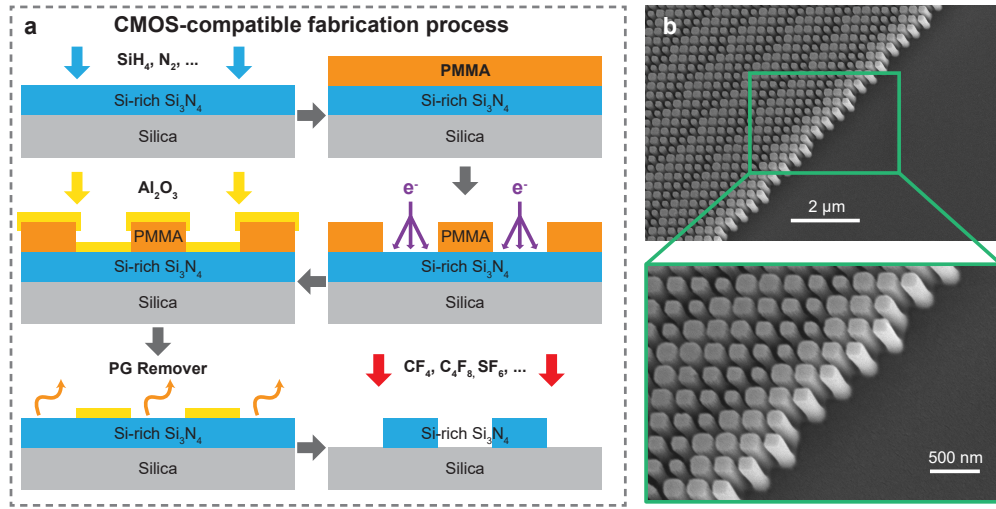
The fabricated metasurfaces feature circular shapes with diameters ranging from 1.16 mm ($4,000 \times 4,000$ pixel resolution with a 290 nm size) to 2.32 mm ($8,000 \times 8,000$ pixel resolution with a 290 nm pixel size). As shown in Extended Data Fig. 3b, the scanning electron microscope (SEM) images of the fabricated samples reveal high-quality SRN nanopillar matrices with minimal defects and clean side walls.

OPTICAL PERFORMANCE OF METASURFACES

The SRN metasurfaces manufactured in this work are large enough to be easily visible by eye (Extended Data Fig. 4). We choose a circular footprint to facilitate alignment with the incident beam. This also reduces unwanted diffraction off the edges of the metasurface.

Metasurfaces have a high forward scattering efficiency, enabling more tweezers to be generated given a fixed input power. The portion of power from the input beam diffracted by the metasurface depends on the input beam shape and the efficiency of the metasurface itself. We choose a beam size slightly larger than the metasurface to ensure a flat intensity profile, which our metasurface design is based on. Therefore, some input power transmits through the substrate without being modulated. We choose an input beam diameter of 1.5 mm for the metasurfaces with 1.16 mm diameter. Excluding the non-overlapped portion of the beam, we observe a diffraction efficiency of 60% into the first order. In the future, the phase mask can be designed for a Gaussian input, allowing the full incident power to be used.

The metasurface platform also has a high power handling capability. We have tested the damage threshold by maximizing the input power and decreasing the waist of the incident beam. Above the threshold, the largest meta-atoms (190 nm) show signs of thermal expansion, closing the air gap that exists between neighboring pillars. We observe the current intensity handling capabilities of the SRN metasurfaces to be up to 25 W/mm^2 , about $5 \times$ larger than the damage threshold of liquid crystal SLMs. By reducing the average pillar size it should



Extended Data Fig. 3. Cleanroom fabrication process and SEM images of SRN metasurfaces. **a**, Illustration of the CMOS-compatible fabrication process. **b**, SEM images of the fabricated SRN metasurfaces show minimal defects and clean side walls.

be possible to improve this threshold further. Also, alternative materials promise even better power handling. For example, we have observed TiO_2 metasurfaces to display no signs of degradation up to 36 W/mm^2 .

Given the measured SRN damage threshold, we provide an estimate for how many traps can realistically be generated with the current parameters. Assuming a $2.3 \text{ mm} \times 2.3 \text{ mm}$ device, 1 mW per trap, and 60% diffraction efficiency, we can in principle generate approximately 80,000 tweezers; therefore, metasurface tweezer arrays with $> 100,000$ sites are realistic without major improvements over our current technology. With modest improvements in the power handling and for device footprints of $10 \text{ mm} \times 10 \text{ mm}$, arrays with $> 1,000,000$ traps are within realistic reach.

Characterizing the uniformity of the metasurface array by measuring the peak optical intensity of each trap, we find a non-uniformity of 4%. This is measured by collimating the metasurface pattern with a single high NA microscope lens, without the full relay optics used in this work. This is notably better than the non-uniformity of 7.5% measured with the atoms. We attribute this discrepancy to imperfections in the relay optics paths. Removal or improvement of the relay optics should allow a 4% non-uniformity of the atomic traps. Of note, we were able to rapidly improve the intensity non-uniformity from an initial 20% to single digit percentages via improvements in the design and fabrication. This uniformity is insensitive to slight misalignment of the incident angle into the metasurface and independent of the pattern geometry.

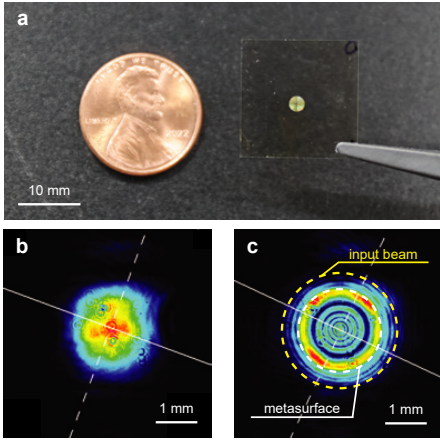
PREPARATION AND IMAGING OF ULTRACOLD STRONTIUM

The preparation of ultracold strontium atoms starts with the generation of a cold atomic beam with a 2D magneto-optical trap (MOT) that is directly loaded from resistively heated dis-

pensers, as described in previous work [61]. The atoms are transferred to a glass cell vacuum chamber via a push-beam where they are captured and cooled to about 1 mK by a 3D MOT operating on the 461 nm transition. We simultaneously operate two repump lasers at 679 nm and 707 nm to close a loss channel present in the 461 nm cooling scheme. To further cool the atoms, we then operate a second MOT on the narrow-line 689 nm transition. We begin the transfer between MOTs by frequency broadening the 689 nm line to 3 MHz to match the temperature distribution of the 461 nm MOT, before smoothly narrowing down to a single-frequency 689 nm MOT with on average 10^5 atoms at 1 μK .

From the ultracold strontium gas, we typically load optical tweezer arrays at a trap depth of 100 μK . The trapping light is provided by a 520 nm 5W fiber laser with second harmonic generation (Azurlight, ALS-GR-520-5-A-CP-SF), seeded by a home-built extended cavity diode laser operating at 1040 nm (QPhotonics, QLD-1030-100S). Directly after the 520 nm laser output, we use an acousto-optic modulator to dynamically control the trap depth of the tweezers. In front of the metasurface, we use a magnifying telescope to increase the beam waist to be larger than the area of the metasurface. After the metasurface, a high-power capable microscope lens (NA = 0.6, Thorlabs, LMH-50X-532) is used to collimate the generated pattern. The tweezer pattern is relayed through a 1:1 telescope before being focused down onto the atoms via an objective lens (NA = 0.5, Mitutoyo, G Plan Apo 50X).

To detect the atomic occupation of the tweezer array, we perform fluorescence imaging. We resonantly scatter photons on the 461 nm transition for 50 ms, collect the fluorescence through the high NA objective that focuses the tweezers, separate the light from the tweezer path via a long-pass dichroic, and image on an EMCCD camera (Andor iXon Ultra 888). We image with a 200 mm lens before the camera, such that a single camera pixel corresponds to a real space size of $260 \text{ nm} \times 260 \text{ nm}$.



Extended Data Fig. 4. Real image of a metasurface and the beam profile after diffraction. **a**, Real size comparison between an American one-cent coin and a 2.32 mm \times 2.32 mm metasurface. **b**, The profile of a 1.5 mm diameter beam that is incident onto the metasurface. **c**, Far-field imaging of non-diffracted light after aligning the metasurface to the beam. This diagnostic, in tandem with optimizing the diffracted power, ensures our system is well aligned.

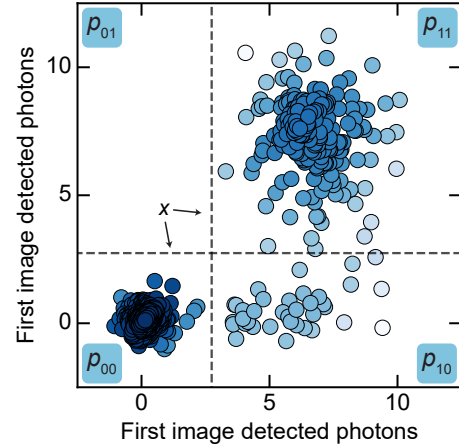
SINGLE-ATOM DETECTION FIDELITY

To determine how well we can distinguish one from zero atoms in a tweezer trap, we use a model-free approach that does not require detailed modeling of the photon counting statistics. Our methodology is similar to the one used in Ref. [48], involving the recording of two fluorescence images of the atom array in short sequence, separated by 25 ms, within the same iteration of the experiment. Besides the detection fidelity, F , it yields the initial filling fraction f and survival rate S of atoms between images.

From the two images, the atomic fluorescence signal (photon count) at each trap location is recorded. For each trap, there are four possible outcomes and associated probabilities: there is an atom in both images (p_{11}), there is an atom in the first but not in the second image (p_{10}), there is an atom in the second but not first image (p_{01}), and there is no atom present in either image (p_{00}). The probability for each event is given by:

$$\begin{aligned} p_{11} &= f(1-F_0)F_1(1-S) + (1-f)(1-F_0)^2 + fF_1^2S, \\ p_{10} &= fF_1S(1-F_1) + fF_1(1-S)F_0 + (1-f)(1-F_0)F_0, \\ p_{01} &= f(1-F_0)(1-F_1)(1-S) + (1-f)(1-F_0)F_0 \\ &\quad + f(1-F_1)F_1S, \\ p_{00} &= 1 - (p_{11} + p_{10} + p_{01}), \end{aligned}$$

where F_0 denotes the detection fidelity for zero atoms, F_1 the detection fidelity of one atom, S is the survival rate between images, and f the initial filling fraction. Initially, the threshold photon count x that marks the distinction between zero and one atom is a variable. By iteratively varying x (see Extended Data Fig. 5), we solve the above equations to maximize the total imaging fidelity defined by $F = fF_1 + (1-f)F_0$. By optimizing the threshold x for each individual tweezer, we find a



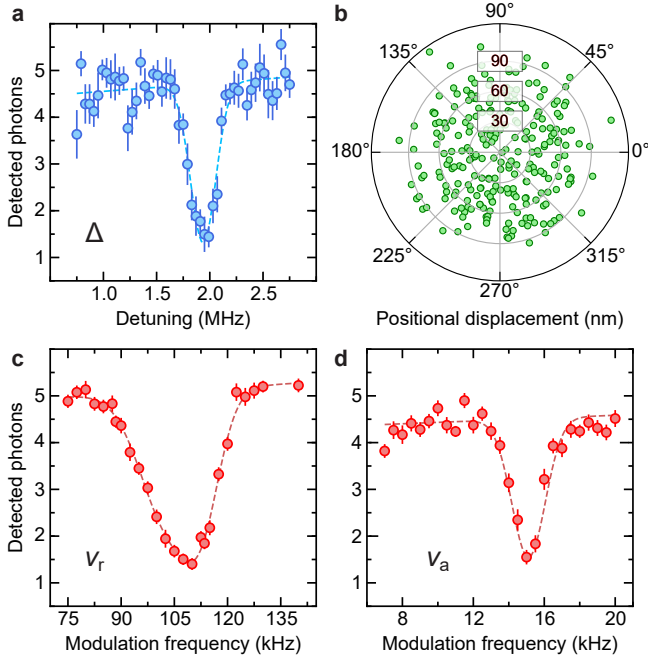
Extended Data Fig. 5. Determination of the photon count threshold x to distinguish between zero and one atom in a trap. Data points show the counts for one specific trap of the 4×4 array in 500 iterations of the experiment. A darker color of the data points indicates a higher density of points. The threshold value x divides the data into four quadrants, labeled by p_{ij} with indices $i = 0, 1$ and $j = 0, 1$ indicating the absence (presence) of an atom in the first and second image, respectively.

mean detection fidelity across the array of $F = 99.8\%$, a mean survival rate of 84.1%, and a mean filling fraction of 49.2%. The reduced survival rate S is attributed to an enhanced loss process associated with the 520 nm trapping wavelength (see main text).

TRAP CHARACTERIZATION

The trap depth is measured via the light shift on the trapped atoms induced by the trapping laser. We probe the light shift on the $m_j = \pm 1$ transition between the 1S_0 and 3P_1 states using the 689 nm MOT beams. When the probe light is resonant with the shifted resonance, the atoms are heated out of the trap. Extended Data Fig. 6a shows a typical loss resonance in an individual trap. Fitting the resonance feature with a Gaussian model, we determine the detuning Δ from the free space resonance. From this we obtain the trap depth $U = \Delta\alpha_{^1S_0}/(\alpha_{^3P_1} - \alpha_{^1S_0})$, where $\alpha_{^1S_0}$ ($\alpha_{^3P_1}$) is the polarization of the 1S_0 (3P_1) state.

The positional accuracy of the tweezer array is extracted by comparing the measured trap locations with the target trap positions that were used for the design of the metasurface. The trap locations are obtained by fitting each atom's fluorescence signal to a 2D Gaussian. The orientation of the metasurface is not fixed to the lab frame and can rotate freely. We minimize the averaged distance between the measured and target trap locations by rotating and translating the coordinate pattern. Following this optimization, we find that the mean deviation of trap locations is 60 nm. As shown in Extended Data Fig. 6b the deviations between measured and target locations are uniformly distributed in all directions, indicating that there is no systematic bias.



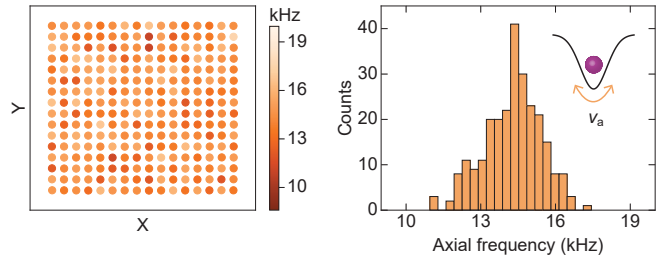
Extended Data Fig. 6. Measurements of uniformity in the 16×16 array. **a**, Measurement of the trap depth via the light shift Δ of the $^1S_0 - ^3P_1$ resonance in the presence of the trapping field. Data shows the resonance for a single trap. **b**, Positional displacement between observed and target trap locations. **c-d**, show the measurement of the radial and axial trap frequency, respectively, via parametric heating. All error bars in this figure show 1σ s.e.m. from 20 repetitions of the measurement.

The trap frequencies are measured via parametric heating. Individual trap loss features at twice the radial and axial trap frequencies are shown in Extended Data Figs. 6c and d, respectively. The parametric resonance in the radial direction shows a slight asymmetry. There are two distinct trap frequencies in the radial direction, which we attribute to the trapping potential not being perfectly circularly symmetric. We fit the line shape with a double Gaussian and plot the geometric mean as the radial trap frequency. The parametric resonance in the axial direction shows a symmetric dip, which we fit with a single Gaussian. Extended Data Fig. 7 shows the axial trap frequencies in each trap and their statistical spread.

EFFECTIVE NA OF PIXEL-BASED BEAM SHAPING DEVICES

The numerical aperture (NA) measures the angular range within which an optical element, for example, a lens, can accept light from a point source. For a spherical lens in vacuum, the NA is given by $\sin \theta$, where θ is the half-angle of the acceptance cone of the lens with $\theta = \arctan(D/(2f))$, where D is the diameter of the lens and f its focal length.

We use the example of a lens to derive an analytical expression for the effective NA of a pixel-based beam shaping device (see Fig. 5a). In the first step, we reduce the phase



Extended Data Fig. 7. Axial trap frequency measurements. The axial trap frequencies measured in a 16×16 with $4 \mu\text{m}$ trap spacing (left) and their statistical spread (right).

profile of the lens with focal length f to a Fresnel lens with continuous local phase shifts, modulo 2π . When we approximate the phase profile of the Fresnel lens $\phi(x)$ with a pixel-based device, the finite sampling limits how well the steep phase gradients at the edge of the lens can be captured. We assume that the phase jumps between neighboring pixels should not be larger than $\pi/2$ to faithfully reproduce the behavior of the lens. For a device with pixel size d , this limits the phase gradient to $\partial\phi/\partial x \lesssim \pi/2d$. The larger the pixel size d relative to wavelength λ , the smaller the phase gradient that can be faithfully captured. As the phase profile of a lens has the steepest gradients near the edge, the usable diameter of the pixel-based device is effectively reduced when gradients near the edge cannot be reproduced.

To derive the dependence of the effective NA on pixel size d and wavelength λ , we consider the following (see Extended Data Fig. 8): We treat each individual pixel of the device as a point scatterer which, following Huygens' principle, creates a radial wavefront with a phase shift corresponding to the phase of a given pixel. We define θ_m as the maximal angle for which the device can faithfully reproduce the phase gradient near the edge. At this angle the phase difference between neighboring pixels reaches $\pi/2$. In terms of wave propagation, this corresponds to a $\lambda/4$ wavefront advance between the neighboring pixels that are spaced by distance d . The effective NA is given by $\sin \theta_m$.

Using the construction of Extended Data Figs. 8a and b and defining the angular separation $\Delta\theta$ between neighboring pixels, the following relations hold:

$$f(\cos(\theta_m) - \cos(\theta_m + \Delta\theta)) = \lambda/4, \\ f(\sin(\theta_m + \Delta\theta) - \sin(\theta_m)) = d.$$

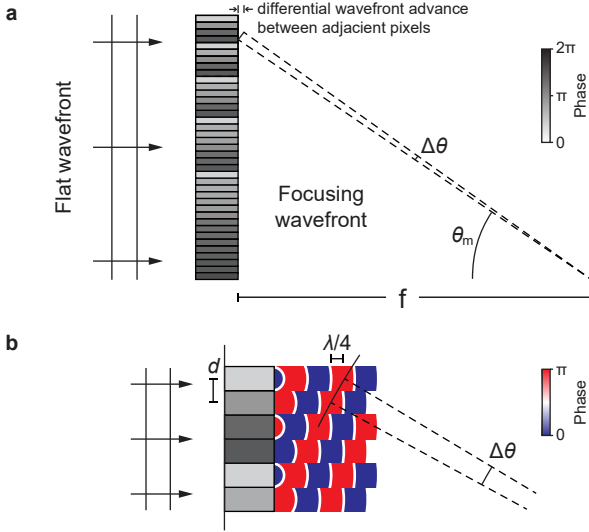
Regrouping the terms yields

$$\cos(\theta_m + \Delta\theta) = \cos \theta_m - \lambda/(4f), \\ \sin(\theta_m + \Delta\theta) = \sin \theta_m + d/f.$$

Squaring both equations and adding them together gives

$$(d/f)^2 + (\lambda/(4f))^2 + (\lambda/2f) \cos \theta_m - (2d/f) \sin \theta_m = 0.$$

As the pixel size and wavelength are much smaller than the focal length, $d, \lambda \ll f$, we neglect the terms quadratic in d/f and λ/f . From this we obtain the relation $\cos \theta_m =$



Extended Data Fig. 8. Calculation of the effective NA of a pixel-based beam shaping device. **a**, The phase profile of a lens with focal length f is emulated by a pixelated phase mask. The individual pixels have a size d . A flat wavefront impinges on the device and it is converted into a focusing wavefront. θ_m is the maximal angle for which the phase advance between neighboring pixels stays smaller than $\pi/2$. The gray scale indicates the phase shift of the metasurface pixels. **b**, Zooming into the wavefront advance of individual pixels, following Huygens' principle, the angle θ_m is determined by the pixel where the wavefront advance between neighboring pixels reaches $\lambda/4$ (corresponding to a phase shift of $\pi/2$). $\Delta\theta$ denotes the angular separation between neighboring pixels. The color scale indicates the phase shift of the emerging wavefront behind the metasurface.

$(4d/\lambda) \sin \theta_m$. Using the definition for the effective NA, this yields

$$\text{NA} = \frac{1}{\sqrt{1 + (4d/\lambda)^2}}.$$

Based on this relation, we can distinguish three regimes (see Fig. 5b):

$d \gg \lambda$: The pixel size is too large to capture steep phase gradients. The lens is only faithfully reconstructed in the paraxial region at the center, leading to an effective NA close to 0.

$d \approx \lambda$: The effective NA sensitively depends on the ratio of pixel size and wavelength d/λ . A small reduction of d/λ can dramatically increase the effective NA.

$d \ll \lambda$: The pixel size is so small that almost any phase gradients can be reproduced, giving rise to an effective NA close to 1.

For our metasurface, $d/\lambda \sim 0.6$ and the effective NA calculated within this simplified model is 0.41, while the actual NA for our metasurfaces is 0.6. Thanks to the high NA, holographic metasurfaces can directly generate diffraction-limited traps on the micrometer scale in their image plane. For current liquid crystal SLMs, the effective NA is 0.05 or less due to their relatively large pixel size (4 μm – 20 μm). They require

high quality demagnification optics with a high NA to realize tweezer arrays on the micrometer scale. Such optics can act as an unintended low-pass filter, cutting off high-frequency spatial Fourier components, posing a challenge to generate uniform and well-resolved tweezer arrays. While such issues can be partially mitigated by iterative optimization of the SLM pattern, holographic metasurfaces offer a way to fundamentally circumvent such issues.

ARRAY SIMULATIONS FOR PIXEL-BASED BEAM SHAPING DEVICES

To numerically simulate the holographic performance of pixel-based beam shaping devices, we employ a Fast Fourier Transform (FFT)-based numerical method to solve the Rayleigh-Sommerfeld diffraction integral for a given phase-only hologram with specified pixel size and resolution. This method has been highly effective in designing optimal phase-only holograms and we have found excellent agreement with our experimental results. We analyze holograms with varying pixel sizes, starting with the smallest pixel size of a commercially available liquid crystal SLM (3.74 μm , GAEA-2 SLM from HOLOEYE Photonics AG) and extending down to the subwavelength pixel size of the metasurfaces used in this work (290 nm). For each pixel size, the hologram is set to a fixed resolution of 300×300 pixels. The position of the focal plane is calculated based on the hologram's physical size ($300d \times 300d$) and the effective NA. Each hologram is optimized using the modified Gerchberg-Saxton algorithm to generate a 3×3 square array of traps with 5 μm spacing in the focal plane without intermediate optics. The optimized hologram serves as the input for the final propagation step in our simulation. By averaging the full width at half maximum (FWHM) values along the x and y axes (assuming the optical axis is along z axis) of the optical intensity profile for each trap, we extract the average and range of FWHM values across the entire array, as presented in Fig. 5c. Our results demonstrate that subwavelength pixel sizes enable the direct generation of diffraction-limited traps with FWHMs smaller than the working wavelength.

The trends of the numerical data are well captured by the analytic effective NA relation derived above. The FWHM of a single trap is related to the NA via $\text{FWHM} = 0.51\lambda/\text{NA}$. Using the effective NA relation derived above and multiplying by a scaling factor α , we obtain the fit function

$$\text{FWHM} = \alpha \times 0.51\lambda \sqrt{1 + (4d/\lambda)^2}.$$

With the scaling factor α being the only free parameter, this model is in excellent agreement with the numerical simulation results (see Fig. 5c).

Furthermore, we numerically investigate the achievable uniformity of trap intensities while increasing the array size. We calculate the normalized standard deviation of trap intensities as a function of the number of generated tweezers in the focal plane for device resolutions ranging from 1000×1000 to $16,000 \times 16,000$ pixels. The simulation assumes a pixel size

of $d = 290$ nm and an NA = 0.6, corresponding to the meta-surfaces used in this work. The position of the focal plane is determined by the hologram size (resolution \times pixel size) and the NA. The holograms are optimized using the algorithm outlined above, and a final forward propagation was performed using the optimized holograms to simulate the tweezer array formed in the focal plane. We integrate the intensity profile

for each tweezer and calculate the standard deviation for the entire array based on these values.

As shown in Fig. 5d, we find that for each resolution, the uniformity starts to decay rapidly beyond a certain number of tweezers. From the data we find empirically that at least 300 pixels per tweezer trap are needed to maintain a uniformity $> 95\%$.

[1] A. M. Kaufman and K.-K. Ni, Quantum science with optical tweezer arrays of ultracold atoms and molecules, *Nat. Phys.* **17**, 1324–1333 (2021).

[2] A. Browaeys and T. Lahaye, Many-body physics with individually controlled Rydberg atoms, *Nat. Phys.* **16**, 132 (2020).

[3] M. Saffman, T. G. Walker, and K. Mølmer, Quantum information with Rydberg atoms, *Rev. Mod. Phys.* **82**, 2313–2363 (2010).

[4] M. Morgado and S. Whitlock, Quantum simulation and computing with Rydberg-interacting qubits, *AVS Quantum Sci.* **3** (2021).

[5] P. Scholl, M. Schuler, H. J. Williams, A. A. Eberharter, D. Barredo, K.-N. Schymik, V. Lienhard, L.-P. Henry, T. C. Lang, T. Lahaye, A. M. Läuchli, and A. Browaeys, Quantum simulation of 2D antiferromagnets with hundreds of Rydberg atoms, *Nature* **595**, 233–238 (2021).

[6] G. Semeghini, H. Levine, A. Keesling, S. Ebadi, T. T. Wang, D. Bluvstein, R. Verresen, H. Pichler, M. Kalinowski, R. Sama-jdar, A. Omran, S. Sachdev, A. Vishwanath, M. Greiner, V. Vuletić, and M. D. Lukin, Probing topological spin liquids on a programmable quantum simulator, *Science* **374**, 1242 (2021).

[7] I. S. Madjarov, J. P. Covey, A. L. Shaw, J. Choi, A. Kale, A. Cooper, H. Pichler, V. Schkolnik, J. R. Williams, and M. Endres, High-fidelity entanglement and detection of alkaline-earth Rydberg atoms, *Nat. Phys.* **16**, 857–861 (2020).

[8] T. M. Graham, Y. Song, J. Scott, C. Poole, L. Phuttitarn, K. Jooya, P. Eichler, X. Jiang, A. Marra, B. Grinkemeyer, M. Kwon, M. Ebert, J. Cherek, M. T. Lichtman, M. Gillette, J. Gilbert, D. Bowman, T. Ballance, C. Campbell, E. D. Dahl, O. Crawford, N. S. Blunt, B. Rogers, T. Noel, and M. Saffman, Multi-qubit entanglement and algorithms on a neutral-atom quantum computer, *Nature* **604**, 457–462 (2022).

[9] S. Ma, G. Liu, P. Peng, B. Zhang, S. Jandura, J. Claes, A. P. Burgers, G. Pupillo, S. Puri, and J. D. Thompson, High-fidelity gates and mid-circuit erasure conversion in an atomic qubit, *Nature* **622**, 279 (2023).

[10] D. Bluvstein, S. J. Evered, A. A. Geim, S. H. Li, H. Zhou, T. Manovitz, S. Ebadi, M. Cain, M. Kalinowski, D. Hangleiter, J. P. Bonilla Ataides, N. Maskara, I. Cong, X. Gao, P. Sales Rodriguez, T. Karolyshyn, G. Semeghini, M. J. Gullans, M. Greiner, V. Vuletić, and M. D. Lukin, Logical quantum processor based on reconfigurable atom arrays, *Nature* **626**, 58 (2024).

[11] K. Singh, S. Anand, A. Pocklington, J. T. Kemp, and H. Bernien, Dual-element, two-dimensional atom array with continuous-mode operation, *Phys. Rev. X* **12** (2022).

[12] C. Sheng, J. Hou, X. He, K. Wang, R. Guo, J. Zhuang, B. Mamat, P. Xu, M. Liu, J. Wang, and M. Zhan, Defect-free arbitrary-geometry assembly of mixed-species atom arrays, *Phys. Rev. Lett.* **128** (2022).

[13] Y. Bao, S. S. Yu, L. Anderegg, E. Chae, W. Ketterle, K.-K. Ni, and J. M. Doyle, Dipolar spin-exchange and entanglement between molecules in an optical tweezer array, *Science* **382**, 1138 (2023).

[14] C. M. Holland, Y. Lu, and L. W. Cheuk, On-demand entanglement of molecules in a reconfigurable optical tweezer array, *Science* **382**, 1143 (2023).

[15] I. S. Madjarov, A. Cooper, A. L. Shaw, J. P. Covey, V. Schkolnik, T. H. Yoon, J. R. Williams, and M. Endres, An atomic-array optical clock with single-atom readout, *Phys. Rev. X* **9**, 041052 (2019).

[16] A. W. Young, W. J. Eckner, W. R. Milner, D. Kedar, M. A. Norcia, E. Oelker, N. Schine, J. Ye, and A. M. Kaufman, Half-minute-scale atomic coherence and high relative stability in a tweezer clock, *Nature* **588**, 408–413 (2020).

[17] Z. Yan, J. Ho, Y.-H. Lu, S. J. Masson, A. Asenjo-Garcia, and D. M. Stamper-Kurn, Superradiant and subradiant cavity scattering by atom arrays, *Phys. Rev. Lett.* **131** (2023).

[18] A. Asenjo-Garcia, M. Moreno-Cardoner, A. Albrecht, H. J. Kimble, and D. E. Chang, Exponential improvement in photon storage fidelities using subradiance and “selective radiance” in atomic arrays, *Phys. Rev. X* **7** (2017).

[19] R. Holzinger, J. S. Peter, S. Ostermann, H. Ritsch, and S. Yelin, Harnessing quantum emitter rings for efficient energy transport and trapping, *Optica Quantum* **2**, 57 (2024).

[20] S. J. Masson, J. P. Covey, S. Will, and A. Asenjo-Garcia, Dicke superradiance in ordered arrays of multilevel atoms, *PRX Quantum* **5** (2024).

[21] J. Grotti, S. Koller, S. Vogt, S. Häfner, U. Sterr, C. Lisdat, H. Denker, C. Voigt, L. Timmen, A. Rolland, F. N. Baynes, H. S. Margolis, M. Zampaolo, P. Thoumany, M. Pizzocaro, B. Rauf, F. Bregolin, A. Tampellini, P. Barbieri, M. Zucco, G. A. Costanzo, C. Clivati, F. Levi, and D. Calonico, Geodesy and metrology with a transportable optical clock, *Nat. Phys.* **14**, 437–441 (2018).

[22] M. Takamoto, I. Ushijima, N. Ohmae, T. Yahagi, K. Kokado, H. Shinkai, and H. Katori, Test of general relativity by a pair of transportable optical lattice clocks, *Nat. Photonics* **14**, 411–415 (2020).

[23] E. R. Elliott, D. C. Aveline, N. P. Bigelow, P. Boegel, S. Botsi, E. Charron, J. P. D’Incao, P. Engels, T. Estrampe, N. Gaaloul, J. R. Kellogg, J. M. Kohel, N. E. Lay, N. Lundblad, M. Meister, M. E. Mossman, G. Müller, H. Müller, K. Oudrhiri, L. E. Phillips, A. Pichery, E. M. Rasel, C. A. Sackett, M. Sbroscia, W. P. Schleich, R. J. Thompson, and J. R. Williams, Quantum gas mixtures and dual-species atom interferometry in space, *Nature* **623**, 502–508 (2023).

[24] M. Endres, H. Bernien, A. Keesling, H. Levine, E. R. Anschuetz, A. Krajenbrink, C. Senko, V. Vuletic, M. Greiner, and M. D. Lukin, Atom-by-atom assembly of defect-free one-dimensional cold atom arrays, *Science* **354**, 1024–1027 (2016).

[25] A. P. Burgers, S. Ma, S. Saskin, J. Wilson, M. A. Alarcón, C. H. Greene, and J. D. Thompson, Controlling Rydberg excitations using ion-core transitions in alkaline-earth atom-tweezer arrays,

PRX Quantum **3** (2022).

[26] D. Barredo, S. de Léséleuc, V. Lienhard, T. Lahaye, and A. Browaeys, An atom-by-atom assembler of defect-free arbitrary two-dimensional atomic arrays, *Science* **354**, 1021–1023 (2016).

[27] D. Kim, A. Keesling, A. Omran, H. Levine, H. Bernien, M. Greiner, M. D. Lukin, and D. R. Englund, Large-scale uniform optical focus array generation with a phase spatial light modulator, *Opt. Lett.* **44**, 3178 (2019).

[28] Y. Wang, S. Shevate, T. M. Wintermantel, M. Morgado, G. Lochead, and S. Whitlock, Preparation of hundreds of microscopic atomic ensembles in optical tweezer arrays, *npj Quantum Inf.* **6** (2020).

[29] P. Huft, Y. Song, T. M. Graham, K. Jooya, S. Deshpande, C. Fang, M. Kats, and M. Saffman, Simple, passive design for large optical trap arrays for single atoms, *Phys. Rev. A* **105**, 063111 (2022).

[30] L. Pause, L. Sturm, M. Mittenbühler, S. Amann, T. Preuschhoff, D. Schäffner, M. Schlosser, and G. Birkl, Supercharged two-dimensional tweezer array with more than 1000 atomic qubits, *Optica* **11**, 222 (2024).

[31] X. Huang, W. Yuan, A. Holman, M. Kwon, S. J. Masson, R. Gutierrez-Jauregui, A. Asenjo-Garcia, S. Will, and N. Yu, Metasurface holographic optical traps for ultracold atoms, *Prog. Quantum Electron.* **89**, 100470 (2023).

[32] B. H. Fong, J. S. Colburn, J. J. Ottusch, J. L. Visher, and D. F. Sievenpiper, Scalar and tensor holographic artificial impedance surfaces, *IEEE Trans. Antennas Propag.* **58**, 3212–3221 (2010).

[33] N. Yu, P. Genevet, M. A. Kats, F. Aieta, J.-P. Tetienne, F. Capasso, and Z. Gaburro, Light propagation with phase discontinuities: generalized laws of reflection and refraction, *Science* **334**, 333–337 (2011).

[34] X. Ni, N. K. Emani, A. V. Kildishev, A. Boltasseva, and V. M. Shalaev, Broadband light bending with plasmonic nanoantennas, *Science* **335**, 427–427 (2012).

[35] H. A. Atikian, N. Sinclair, P. Latawiec, X. Xiong, S. Meesala, S. Gauthier, D. Wintz, J. Randi, D. Bernot, S. DeFrances, J. Thomas, M. Roman, S. Durrant, F. Capasso, and M. Lončar, Diamond mirrors for high-power continuous-wave lasers, *Nat. Commun.* **13** (2022).

[36] A. Arbabi, Y. Horie, A. J. Ball, M. Bagheri, and A. Faraon, Subwavelength-thick lenses with high numerical apertures and large efficiency based on high-contrast transmitarrays, *Nat. Commun.* **6** (2015).

[37] J. P. Balthasar Mueller, N. A. Rubin, R. C. Devlin, B. Groever, and F. Capasso, Metasurface polarization optics: independent phase control of arbitrary orthogonal states of polarization, *Phys. Rev. Lett.* **118** (2017).

[38] H. Huang, A. C. Overvig, Y. Xu, S. C. Malek, C.-C. Tsai, A. Alù, and N. Yu, Leaky-wave metasurfaces for integrated photonics, *Nat. Nanotechnol.* **18**, 580 (2023).

[39] T.-W. Hsu, W. Zhu, T. Thiele, M. O. Brown, S. B. Papp, A. Agrawal, and C. A. Regal, Single-atom trapping in a metasurface-lens optical tweezer, *PRX Quantum* **3**, 030316 (2022).

[40] N. Yu and F. Capasso, Flat optics with designer metasurfaces, *Nat. Mater.* **13**, 139–150 (2014).

[41] W. T. Chen, A. Y. Zhu, and F. Capasso, Flat optics with dispersion-engineered metasurfaces, *Nat. Rev. Mater.* **5**, 604 (2020).

[42] A. V. Kildishev, A. Boltasseva, and V. M. Shalaev, Planar photonics with metasurfaces, *Science* **339** (2013).

[43] J.-S. Park, S. W. D. Lim, A. Amirzhan, H. Kang, K. Karrfalt, D. Kim, J. Leger, A. Urbas, M. Ossiander, Z. Li, and F. Capasso, All-glass 100 mm diameter visible metalens for imaging the cosmos, *ACS Nano* **18**, 3187–3198 (2024).

[44] T. Zelevinsky, M. M. Boyd, A. D. Ludlow, T. Ido, J. Ye, R. Ciuryło, P. Naidon, and P. S. Julienne, Narrow line photoassociation in an optical lattice, *Phys. Rev. Lett.* **96** (2006).

[45] A. Cooper, J. P. Covey, I. S. Madjarov, S. G. Porsey, M. S. Safronova, and M. Endres, Alkaline-earth atoms in optical tweezers, *Phys. Rev. X* **8** (2018).

[46] F. Gyger, M. Ammenwerth, R. Tao, H. Timme, S. Snigirev, I. Bloch, and J. Zeiher, Continuous operation of large-scale atom arrays in optical lattices, *Phys. Rev. Res.* **6**, 033104 (2024).

[47] J. P. Covey, I. S. Madjarov, A. Cooper, and M. Endres, 2000-times repeated imaging of strontium atoms in clock-magic tweezer arrays, *Phys. Rev. Lett.* **122**, 173201 (2019).

[48] M. A. Norcia, A. W. Young, and A. M. Kaufman, Microscopic control and detection of ultracold strontium in optical-tweezer arrays, *Phys. Rev. X* **8** (2018).

[49] F. Nogrette, H. Labuhn, S. Ravets, D. Barredo, L. Béguin, A. Vernier, T. Lahaye, and A. Browaeys, Single-atom trapping in holographic 2D arrays of microtraps with arbitrary geometries, *Phys. Rev. X* **4**, 021034 (2014).

[50] H. J. Manetsch, G. Nomura, E. Bataille, K. H. Leung, X. Lv, and M. Endres, A tweezer array with 6100 highly coherent atomic qubits, *arXiv:2403.12021* (2024).

[51] K.-N. Schymik, B. Ximenez, E. Bloch, D. Dreon, A. Signoles, F. Nogrette, D. Barredo, A. Browaeys, and T. Lahaye, In situ equalization of single-atom loading in large-scale optical tweezer arrays, *Phys. Rev. A* **106**, 022611 (2022).

[52] Y. T. Chew, M. Poitinal, T. Tomita, S. Kitade, J. Mauricio, K. Ohmori, and S. de Léséleuc, Ultra-precise holographic optical tweezers array, *arXiv:2407.20699* (2024).

[53] S. C. Malek, A. C. Overvig, A. Alù, and N. Yu, Multifunctional resonant wavefront-shaping meta-optics based on multilayer and multi-perturbation nonlocal metasurfaces, *Light Sci. Appl.* **11**, 246 (2022).

[54] M. Khorasaninejad, W. T. Chen, R. C. Devlin, J. Oh, A. Y. Zhu, and F. Capasso, Metalenses at visible wavelengths: diffraction-limited focusing and subwavelength resolution imaging, *Science* **352**, 1190 (2016).

[55] Y. Wu, W. Yang, Y. Fan, Q. Song, and S. Xiao, TiO₂ metasurfaces: from visible planar photonics to photochemistry, *Sci. Adv.* **5**, eaax0939 (2019).

[56] S. C. Malek, Y. Xu, and N. Yu, Visible-spectrum wavelength-selective metalenses based on quasi-bound states in the continuum, in *CLEO 2023* (IEEE, 2023) pp. 1–2.

[57] H. Nejadriahi, A. Friedman, R. Sharma, S. Pappert, Y. Fainman, and P. Yu, Thermo-optic properties of silicon-rich silicon nitride for on-chip applications, *Opt. Express* **28**, 24951 (2020).

[58] R. W. Gerchberg and W. O. Saxton, A practical algorithm for the determination of phase from image and diffraction plane pictures, *Optik* **35**, 237 (1972).

[59] M. Johansson and J. Bengtsson, Robust design method for highly efficient beam-shaping diffractive optical elements using an iterative-Fourier-transform algorithm with soft operations, *J. Mod. Opt.* **47**, 1385 (2000).

[60] R. Di Leonardo, F. Ianni, and G. Ruocco, Computer generation of optimal holograms for optical trap arrays, *Opt. Express* **15**, 1913 (2007).

[61] M. Kwon, A. Holman, Q. Gan, C.-W. Liu, M. Molinelli, I. Stevenson, and S. Will, Jet-loaded cold atomic beam source for strontium, *Rev. Sci. Instrum.* **94** (2023).